coatings

MDPI

Article

Study on the Formation Mechanism of Serrated Chips in the Cutting Process of Powder Metallurgy Superalloys Based on a Modified J–C Constitutive Relation Simulation Model

Xiaoping Ren [1,2,3,*], Chen Ling [1,2,3], Xuepeng Wang [1,2,3], Yinghao Li [1,2,3], Zhanqiang Liu [1,2,3] and Bing Wang [1,2,3]

[1] School of Mechanical Engineering, Shandong University, Jinan 250061, China; topbot@163.com (C.L.); sduwangxuepeng@mail.sdu.edu.cn (X.W.); sduliyinghao@mail.sdu.edu.cn (Y.L.)
[2] Key National Demonstration Center for Experimental Mechanical Engineering Education, Jinan 250061, China
[3] Key Laboratory of High Efficiency and Clean Mechanical Manufacture of MQE, Jinan 250061, China
* Correspondence: renxiaoping@sdu.edu.cn; Tel.: +86-531-88392329

Abstract: Powder metallurgy superalloys are attracting great attention due to their unique performance advantages, such as good oxidation resistance, corrosion resistance, excellent tensile behavior, durability, fatigue properties, and long-term tissue stability. Therefore, powder superalloys show strong vitality in the field of advanced aerospace engines. However, the cutting force is large, and the serrated chips lead to poor machinability in the cutting process. The influence of dynamic recrystallization softening on serrated chips in the cutting process cannot be ignored. In this paper, the formation mechanism of serrated chips in the FGH96 cutting process is studied considering the influence of dynamic recrystallization softening. Firstly, based on the J–C constitutive relation modified by the recrystallization stress softening established previously, a finite element simulation model of the right-angle cutting of FGH96 is established. According to the results of the simulation model, the variation law of the thermal mechanical loading field in the formation process of serrated chips is quantitatively characterized. The validity of the simulation model is verified by comparison with the cutting force, chip morphology, and strain rate obtained from the experiment. Simulation results show that, in the formation process of serrated chips, the temperature field, strain field, and strain rate field in the first deformation zone show similar distribution characteristics to the shear band distribution, and with the formation of serrated chips, their values gradually increase. On this basis, the formation mechanism of serrated chips is revealed, which is the stage of serrated chip initiation, the stage of generating 50% serrated chips, the stage of generating 75% serrated chips, and the stage of serrated chip formation.

Keywords: serrated chip; powder metallurgy superalloy; modified constitutive model; cutting simulation

Citation: Ren, X.; Ling, C.; Wang, X.; Li, Y.; Liu, Z.; Wang, B. Study on the Formation Mechanism of Serrated Chips in the Cutting Process of Powder Metallurgy Superalloys Based on a Modified J–C Constitutive Relation Simulation Model. *Coatings* **2024**, *14*, 933. https://doi.org/10.3390/coatings14080933

Academic Editor: Francesco Di Quarto

Received: 29 June 2024
Revised: 17 July 2024
Accepted: 22 July 2024
Published: 25 July 2024

1. Introduction

Powder metallurgy superalloys have become the preferred materials for hot-end components of aero-engines because of their excellent performance under high-temperature conditions [1]. However, due to the characteristics of the low plasticity and poor thermal conductivity of powder metallurgy superalloys, temperature accumulation in the cutting deformation zone is fast, the tool wear is serious, and the controllability of the machined surface quality is poor in the subsequent cutting process [2,3].

The study of chip morphology and its formation mechanism is helpful to better understand the metal cutting process, which is of great significance to improve the machinability and surface quality of the workpiece [4]. In the cutting process, the powder metallurgy superalloy experiences severe plastic deformation. The shear, extrusion, and friction phenomena in the cutting deformation zone provide the driving force for the rapid dynamic recrystallization nucleation of the processed material [5]. The above behavior leads to the

unstable thermoplasticity of the material, which in turn promotes the formation of adiabatic shear bands and finally presents a periodically distributed serrated chip.

Compared with the experimental observation method, finite element simulation technology is an effective means to study the chip formation mechanism [6–8]. The reliability of finite element simulation depends on the definition of the material constitutive model, separation criterion, meshing, etc. [9]. B. Wang [10] analyzed the influence of J–C constitutive equation parameters on the accuracy of the finite element simulation model. The results show that the serrated chip is more sensitive to the coefficients A and m in the constitutive model. Guigen Ye et al. [11] optimized the constitutive equation parameters of titanium alloy by the optimization algorithm, which can more accurately describe the change from continuous chips to discontinuous chips under high-speed cutting. In Tahsin Tecelli Öpöz's study [12], the formation of chips is related to many factors, such as material properties, tool angle, cutting parameters, and so on. In the FEM model of chip formation, a progressive damage model with damage evolution criterion is adopted. In Aydın M's study [13], the importance of mesh setting to the simulation model is proposed, and the influence of mesh parameters on chip formation is analyzed.

In summary, although researchers have conducted a lot of research on finite element simulation technology, how to consider the influence of dynamic recrystallization behavior on chip formation in the cutting process is still a challenge, which is of great significance for a deeper understanding of the formation mechanism of serrated chips. The change of material properties caused by dynamic recrystallization can be incorporated in the constitutive equation [14]. Calamaz et al. [15] considered the influence of strain softening caused by recrystallization on flow stress. By adding a hyperbolic tangent function after the original J–C model and applying it to cutting simulation, the accuracy of low-speed cutting process simulation was improved. The modified model has been extended and applied to low-speed cutting simulation of materials [16,17]. Nithyaraaj K P et al. [18] conducted orthogonal cutting finite element simulation of two modified models, JC-TANH and JC-HOU [19], with the original model and compared the experimental results under various constitutive parameters. It is pointed out that the original model and JC-TANH cannot describe the discontinuous cutting phenomenon under high-speed cutting. Although JC-HOU can accurately describe the chip morphology when discontinuous chips are generated, the model does not consider the effect of recrystallization softening. Therefore, how to modify the constitutive model and establish the finite element model of powder metallurgy superalloys considering dynamic recrystallization behavior has important theoretical significance for analyzing the chip formation mechanism.

In summary, aiming at the problem that the formation mechanism of serrated chips in the cutting process of powder superalloy FGH96 is not clear and based on the established modified constitutive equation, this paper considers the influence of the dynamic recrystallization softening effect on the formation process of serrated chips through the cutting simulation model and reveals the formation mechanism of serrated chips according to the simulation results. Firstly, based on the previous research of the research group [20], this paper establishes a cutting simulation model for powder superalloys. The validity of the simulation model is verified by comparison with the cutting force, chip morphology, and strain rate obtained from the experiment. Secondly, based on the simulation result, the different stages of serrated chip formation are studied, and the thermal–mechanical loading field at different stages is quantitatively analyzed. Finally, the formation mechanism of serrated chips is revealed. This study has good guiding significance for the efficient and high-quality cutting of powder superalloys.

2. Finite Element Simulation Model

To analyze the formation mechanism of serrated chips in the cutting process, the cutting simulation model of FGH96 is established. The main methods of modeling are described in detail below.

2.1. Modified J–C Constitutive Model

The J–C model has been widely used as a cutting simulation model because of its relatively simple form, which is shown in Equation (1).

$$\sigma_{J-C} = (A + B\varepsilon^n)(1 + C\ln\frac{\dot{\varepsilon}}{\dot{\varepsilon}_0})\left[1 - \left(\frac{T - T_0}{T_m - T_0}\right)^m\right] \quad (1)$$

where A is the yield strength, B and n are strain-hardening coefficients, C is the strain rate coefficient, and m is the coefficient of the temperature effect. T_0, $\dot{\varepsilon}_0$, T_m are the reference temperature, the reference strain rate ($\dot{\varepsilon}_0$), and the melting point, respectively. σ, ε, and $\dot{\varepsilon}$ are the true stress, true strain, and true strain rate, respectively.

A modified J–C constitutive model considering the dynamic recrystallization effect proposed in previous research [20] is used in this paper, as shown in Equations (2) and (3).

$$\sigma = \sigma_{J-C} \cdot \left[1 - \left(\frac{h_0}{\varepsilon} + h_1 - (\frac{h_0}{\varepsilon} + h_2)\ln(\frac{\dot{\varepsilon}}{\dot{\varepsilon}_0})\right) \cdot u(\dot{\varepsilon}, T)\right]^{-1}, u(\dot{\varepsilon}, T) = \begin{cases} 0, \varepsilon < \varepsilon_r \\ 1, \varepsilon \geq \varepsilon_r \end{cases} \quad (2)$$

$$\varepsilon_{\mathrm{r}} = r_0 + r_1 \mathrm{T}^{r_2} + r_3 \dot{\varepsilon}^{r_4} + r_5 T^{r_2} \dot{\varepsilon}^{r_4} \quad (3)$$

where in Equation (2), h_i (i = 0, 1, 2) are coefficients to be defined by experimentation. ε_{r} is the critical strain of dynamic recrystallization. $u(\dot{\varepsilon}, T)$ is used as a unified equation. The value of $u(\dot{\varepsilon}, T)$ is set to 1 when recrystallization occurs, and 0 otherwise. In Equation (3), r_i (i = 0, 1, …, 5) is the constant to be defined by fitting the algorithm.

Through the dynamic performance test experiment, the parameters of the modified J–C constitutive equation were solved by the linear fitting method, as shown in Table 1. For the detailed process, refer to the previous work of our group [20].

Table 1. The modified J–C constitutive model parameters [20].

Parameters	Values
A (MPa)	773
B (MPa)	1271
C	0.031
n	0.667
m	$8.05 \times 10^4 \dot{\varepsilon} + 1.66$
h_1	−0.015
h_2	−0.015
h_3	0.046
ε_r	$1.445 - 5.85 \times 10^{-5} T^{1.415} - 0.139\dot{\varepsilon}^{0.215} + 6.45 \times 10^{-6} T^{1.415}\dot{\varepsilon}^{0.215}$

The modified J–C constitutive equation is embedded into the simulation model through the VUHARD subroutine to realize the description of the plastic deformation behavior of FGH96 considering the dynamic recrystallization softening effect.

2.2. Simulation Model

Abaqus software 6.13 was selected to simulate the chip formation process. The simulation orthogonal cutting model consists of a tool model and a workpiece model, as shown in Figure 1. Since the influence of tool wear is not considered, the tool is set as a rigid body. To reduce the mesh distortion of the tool–worker contact area in the simulation model, the rounded corner of the tool is set to 0.01 mm and the chip part is set to a 45° oblique angle structure [18]. The tool is only allowed to move in the direction of the cutting speed, with no displacement along the Y-axis direction. The workpiece model is set to a layered structure, which is a chip layer, a joint layer, and a base layer. The bottom and both sides of the workpiece are completely fixed, limiting its movement along the X-axis and Y-axis directions. The established cutting simulation model and its setting conditions are shown in Figure 1.

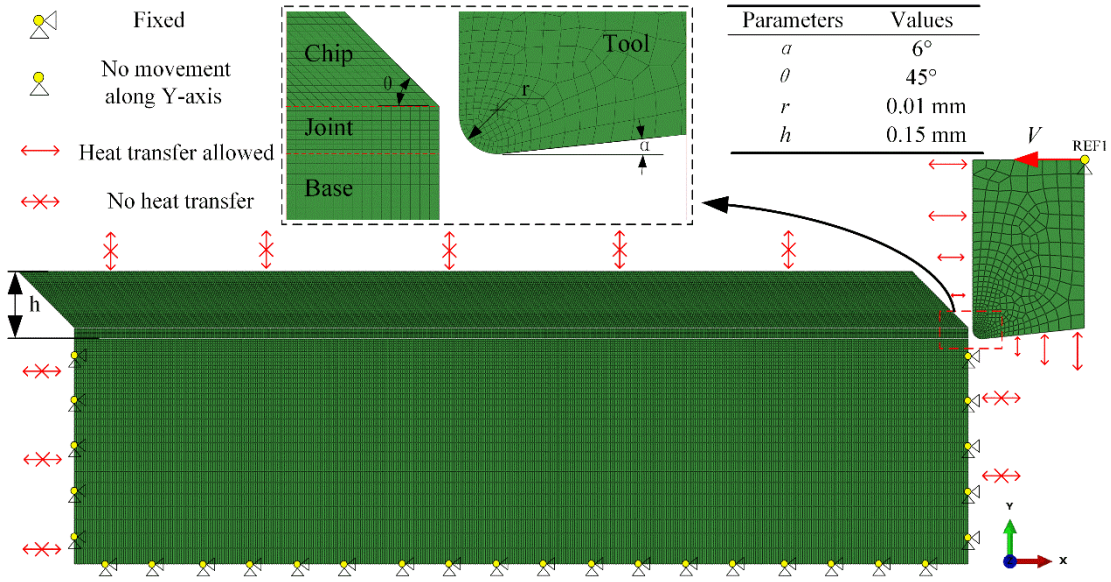

Figure 1. Orthogonal cutting model based on Abaqus.

To improve the efficiency, the grid division adopts the strategy of adapting to local conditions. Smaller quadrilateral grids were used for the cutting area, both for the tool and workpiece, and the standard quadrilateral mesh was used for the other areas. This type of element has higher calculation accuracy and operation speed under the condition of temperature-displacement coupling [21].

The rake angle and clearance angle of the tool is set to 0° and 6°, respectively. The cutting speed range is 60 m/min–120 m/min. In addition, the initial temperature of the model is 25 °C. The mechanical properties of the tool and workpiece are shown in Table 2. Considering the influence of temperature changes on the physical properties of materials, the physical performance of FGH96 at different temperatures is determined, as shown in Table 3.

Table 2. The mechanical properties of the tool and workpiece.

	Density (kg/m^3)	**Elastic Modulus (GPa)**	**Poisson's Ratio**	**Thermal Conductivity (W/(m·°C))**	**Expansion Coefficient × 10^{-5}(/°C)**	**Specific Heat (J/(Kg·°C))**
Tool	15,700	705	0.23	24	0.5	178
Workpiece	8320	220	0.33	9.3	1.11	390

Table 3. Physical performance parameters of FGH96 at different temperatures.

Items	**Parameters**				
Thermal conductivity (W/(m·°C))	9.3 (25 °C)	11.2 (200 °C)	14.0 (400 °C)	17.2 (600 °C)	20.1 (800 °C)
Linear expansion coefficient	1.11 (25 °C)	1.19 (200 °C)	13.3 (400 °C)	14.4 (600 °C)	15.1 (800 °C)
Specific heat (J/(Kg·°C))	390 (25 °C)	420 (200 °C)	455 (400 °C)	487 (600 °C)	520 (800 °C)

The Coulomb friction model is used to describe the frictional contact form of the tool–work contact area. In the slip region, the shear stress (τ) of the tool–chip contact

surface is less than the ultimate shear stress ($\overline{\tau}_{\max}$), and the friction stress (τ_f) in this region is shown in Equation (4). In the bonding area, the shear stress (τ) of the tool–chip contact surface is greater than or equal to the ultimate shear stress ($\overline{\tau}_{\max}$), so the friction stress (τ_f) of the tool–chip contact in this area is shown in Equation (5).

$$\tau_f = \mu\sigma, \tau < \overline{\tau}_{\max} \tag{4}$$

$$\tau_f = \overline{\tau}_{\max}, \tau \geq \overline{\tau}_{\max} \tag{5}$$

where τ_f is the friction stress, μ is the friction coefficient, and $\overline{\tau}_{\max}$ is the ultimate shear stress.

With the accumulation of equivalent plastic strain, the state variable w is introduced to determine the damage to the material, as shown in Equation (6).

$$w = \sum \frac{\Delta\overline{\varepsilon}}{\overline{\varepsilon}_f} \tag{6}$$

where w is the damage state variable, $\Delta\overline{\varepsilon}$ is the incremental equivalent plastic strain, and $\overline{\varepsilon}_f$ is the equivalent damage strain under current conditions. The equivalent damage strain is shown in (7).

$$\overline{\varepsilon}_f = \left(d_1 + d_2 exp d_3 \frac{P}{\overline{\sigma}}\right)\left(1 + d_4 ln \frac{\dot{\overline{\varepsilon}}}{\dot{\overline{\varepsilon}}_0}\right)\left[1 - d_5\left(\frac{T - T_0}{T_m - T_0}\right)^m\right] \tag{7}$$

where P is the mean stress, $\overline{\sigma}$ is Mises stress, $P/\overline{\sigma}$ is expressed as the stress triaxiality, and d_i represents the damage parameters. The damage model parameters of FGH96 are shown in Table 4.

Table 4. Damage parameters of FGH96 [22].

d_1	d_2	d_3	d_4	d_5
−0.239	0.456	0.30	0.07	2.5

3. Orthogonal Cutting Experiment

A right-angle cutting experimental platform is designed to verify the simulation model, which is shown in Figure 2. Based on the three-axis CNC high-speed cutting experimental platform, the measurement of force, chip morphology, and strain rate in orthogonal cutting is realized by adding a dynamometer and DIC (digital image correlation) measurement system. The dynamometer is installed on the Z-axis column (Figure 2a). The workpiece is fixed on a moving platform. The cutter with zero rake angle is selected, and orthogonal cutting is realized when the workpiece is controlled to move rapidly in the Y-axis direction by a computer (Figure 2b).

The powder superalloy FGH96 used in this paper is prepared by the Hot Isostatic Pressing (HIP) + Hot Isostatic Forging (HIF) forming process. The chemical composition of superalloy FGH96 is shown in Table 5. The hardness of FGH96 is 47.5 HRC. The received FGH96 block was machined into a rectangular sample (25 mm × 20 mm × 1.5 mm) by wire cutting. In order to avoid abnormal tool breakage at the beginning of cutting, the starting position of the rectangular sample was processed into a 45° guide angle (Figure 2c). Then, the sample was polished and sandblasted to obtain the results of the DIC system.

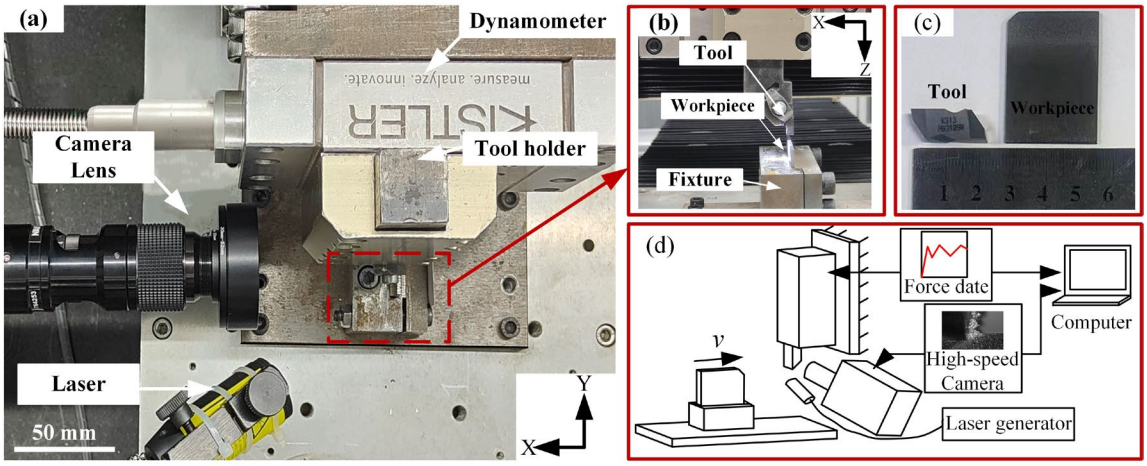

Figure 2. Orthogonal cutting platform. (**a**) Top view; (**b**) Front view; (**c**) Tool and workpiece; (**d**) Schematic diagram.

Table 5. Chemical composition of superalloy FGH96.

Element	C	Al	Ti	Cr	Co	Nb	Mo	W	Ni
Quality fraction (%)	0.02	2.2	3.7	16	13	0.8	4	4	Bal

The DIC system consists of a high-speed camera, camera lens, and laser light source (Figure 2a,d). The parameters of DIC (Correlated Solutions, Inc VRI 's Phantom @ v2012 model, Columbia, SC, USA) are shown in Table 6. To reduce the influence of machine tool vibration, a high-speed camera is installed on a stable bracket at a certain distance from the experiment platform. To improve the clarity under high-speed cutting, a high-frequency pulsed laser source (CAVILU HF of Cavitar, Tampere, Finland) was selected.

Table 6. High-speed camera system parameters.

Items	Parameters	Unit
Lens magnification	9	X
Camera resolution	512 × 320	pixels
Spatial resolution	3	μm/pixel
Frame rate	100,000	FPS
Exposure time	0.19	μs

To ensure that the cutting deformation strictly follows the plane strain, the cutting depth must be within the range of 0.05–0.15 times the workpiece thickness (1.5 mm). In this paper, the experimental cutting depth is set to 0.15 mm.

4. Model Validation

4.1. Cutting Force

A comparison between the simulation result and the experimental result of the instantaneous cutting force when the cutting speed is 60 m/min is performed. Figure 3 is the experimental value of the instantaneous cutting force components (main cutting force F_c, radial force F_p, and axial force F_f). Figure 4 is the predicted value of the instantaneous cutting force components (main cutting force F_c and radial force F_p).

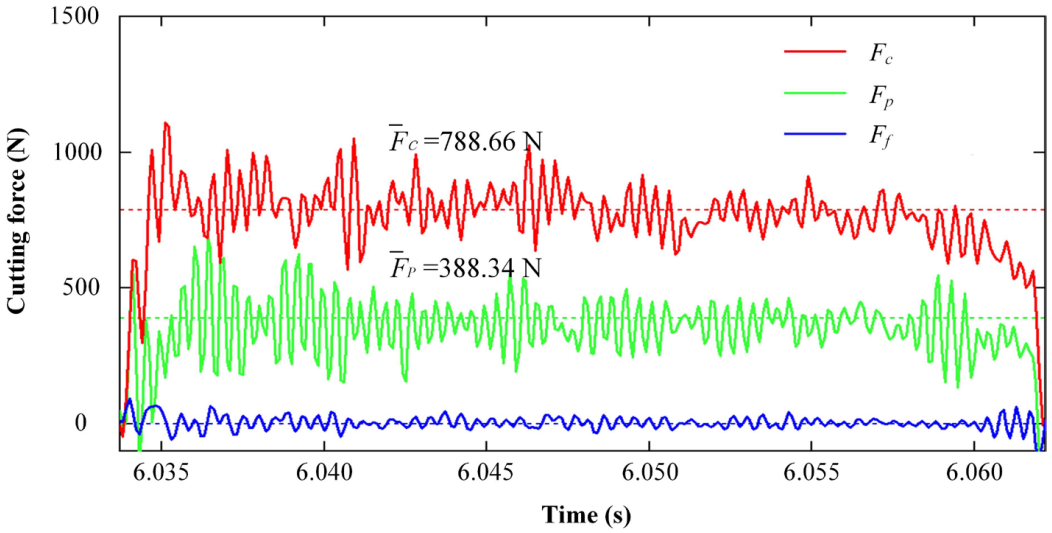

Figure 3. The experiment value of instantaneous cutting force when cutting speed is 60 m/min.

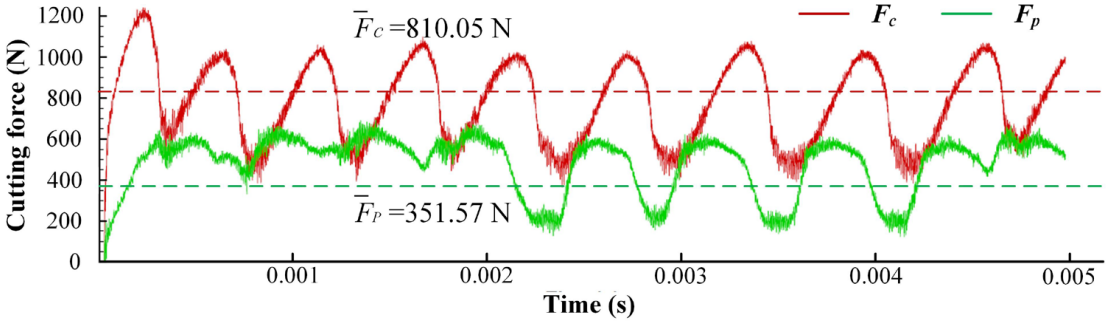

Figure 4. The simulation value of instantaneous cutting force when cutting speed is 60 m/min.

From Figure 3, the experimental value of axial force F_f changes slightly near zero, which proves that the cutting experiment meets the orthogonal requirements. At the cutting speed of 60 m/min, the range of the main cutting force F_c experimental value is 586 N–1112 N, and the range of the radial force F_p experimental value is 149 N–688 N. From Figure 4, the range of the predicted main cutting force F_c is 456 N–1185 N, and the range of the predicted radial force F_p is 138 N–693 N.

The average cutting force of stable cutting (time range is 6.035 s–6.057 s) is compared, as shown in Figure 5. Figure 5a,b are the change trend of the main cutting force and the radial force at different cutting speeds, respectively. From Figure 5, with the increase in cutting speed, the experimental average values of the main cutting force F_c and radial force F_p increase with the increase in cutting speed, and the predicted average values of the main cutting force F_c and radial force F_p show the same trend.

According to the relative error between the simulation and the experimental result, the accuracy of the finite element simulation prediction is quantitatively evaluated. Table 7 shows the experimental average and simulation average of the cutting force and their relative errors. From Table 7, the relative errors between the experimental average and the predicted average of the main cutting force F_c are 2.71%, 3.42%, and 3.63%, respectively, and the relative errors between the experimental average and the predicted average of the radial force F_p are 9.50%, 5.01%, and 4.01%, respectively.

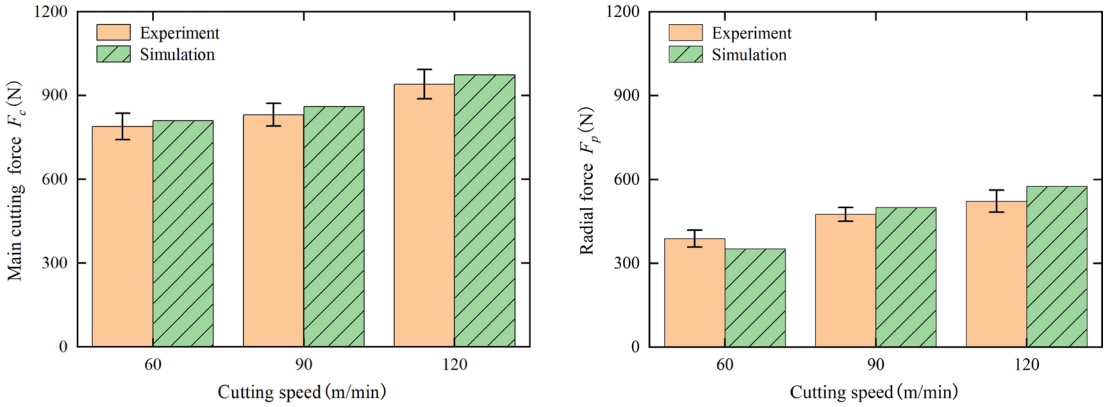

(a) Comparison of Experimental and Simulation main cutting force F_c

(b) Comparison of Experimental and Simulation radial force F_p

Figure 5. Comparison between the experimental average value and the predicted average value of the cutting force at different cutting speeds.

Table 7. Relative errors between the predicted average value and the experimental average value of cutting force.

Cutting Speed v_c (m/min)	Experimental Mean Force		Predict Mean Force.			
	Main Cutting Force F_c (N)	Radial Force F_p (N)	Main Cutting Force F_c (N)	Relative Errors	Radial Force F_p (N)	Relative Errors
60	788.66 ± 47.56	388.34	810.05	2.71%	351.57	9.50%
90	830.94 ± 40.52	475.41	859.36	3.42%	499.21	5.01%
120	940.10 ± 52.45	522.45	926.21	3.63%	574.95	4.01%

4.2. Chip Geometry

Figure 6 shows the chip morphology obtained by the cutting experiment and the simulation model when the cutting speed is 60 m/min. From Figure 5, the chip morphology obtained by the finite element simulation is similar to that of the cutting experiment, both showing a regular sawtooth shape.

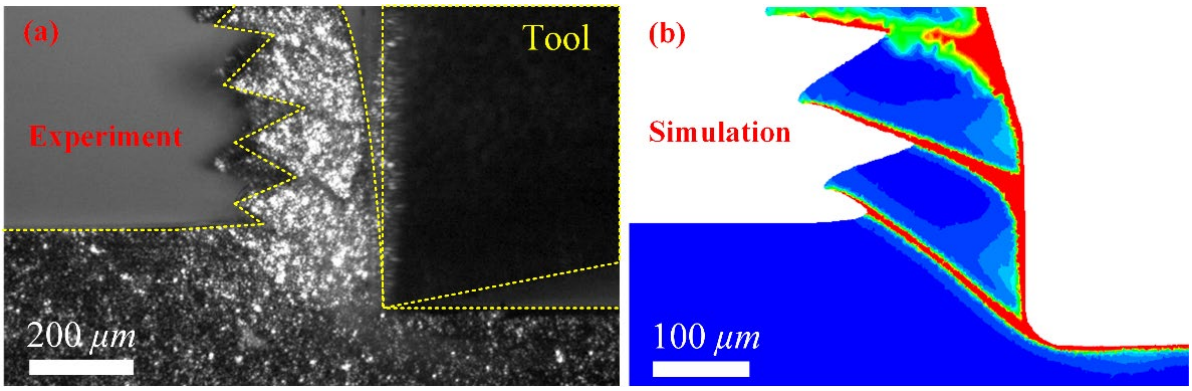

Figure 6. (**a**,**b**) Comparison of chip morphology obtained by experiment and simulation at 60 m/min speed.

Five geometric characterization parameters (tooth addendum height H, tooth valley height h, tooth spacing d, tooth addendum angle α_1, and tooth bottom angle α_2) were selected to characterize chip morphology, and the relative error of the characterization parameters was calculated, as shown in Table 8. The average value of 10 sets of data at each cutting speed is selected as the final chip morphology characterization result.

Table 8. Relative error of chip morphology characterization parameters between finite element simulation and cutting experiment.

Items	Cutting Speed v_c (m/min)	Experiment Values	Predict Values	Relative Errors
tooth addendum height, H (mm)	60	0.271 ± 0.018	0.265	2.21%
	90	0.291 ± 0.023	0.295	2.06%
	120	0.312 ± 0.020	0.319	2.24%
tooth valley height, h (mm)	60	0.157 ± 0.010	0.139	11.4%
	90	0.145 ± 0.012	0.130	10.3%
	120	0.116 ± 0.010	0.121	4.31%
tooth spacing, d (mm)	60	0.108 ± 0.010	0.101	6.48%
	90	0.129 ± 0.011	0.121	6.20%
	120	0.135 ± 0.012	0.139	2.96%
tooth addendum angle, α_1 (°)	60	56.3 ± 3.1	57.4	1.95%
	90	54.4 ± 4.8	55.6	2.21%
	120	51.3 ± 5.2	52.9	3.12%
tooth bottom angle, α_2 (°)	60	65.4 ± 4.1	66.9	2.29%
	90	54.1 ± 4.8	57.0	5.26%
	120	47.5 ± 3.9	49.2	4.82%

According to Table 8, compared with the experimental values of the chip characterization parameters, the maximum relative errors of tooth addendum height H, tooth valley height h, tooth spacing d, tooth addendum angle α_1, and tooth bottom angle α_2 obtained by simulation are 2.24%, 11.4%, 6.48%, 3.12%, and 5.26%, respectively.

In addition, based on the geometric characterization parameters of the chip, the serrated degree G_s and the serrated frequency f of the chip can be obtained according to Equations (8) and (9).

$$Gs = 1 - \frac{h}{H} \tag{8}$$

$$f = \frac{2v_c}{d(H+h)} \tag{9}$$

where v_c is the cutting speed.

Figure 7 is the comparison between the experimental value and the simulation value of the chip serration degree G_s at different cutting speeds. From Figure 7, when the cutting speed increased from 60 m/min to 120 m/min, the relative errors of the chip serration degree G_s obtained by the simulation model are 13.0%, 8.34%, and 1.20%, respectively.

Figure 8 shows the comparison between the experimental result and the simulation result of the chip serration frequency. From Figure 8, when the cutting speed increased from 60 m/min to 120 m/min, the relative errors of the chip serration frequency f obtained by simulation are 13.2%, 12.1%, and 5.53%, respectively.

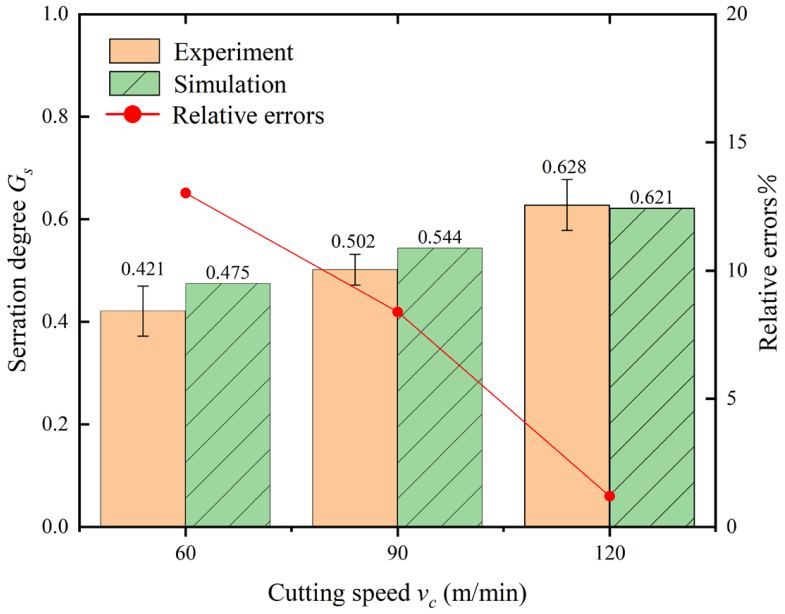

Figure 7. Comparison of serration from the experiment and predicted chip serrated degree G_s.

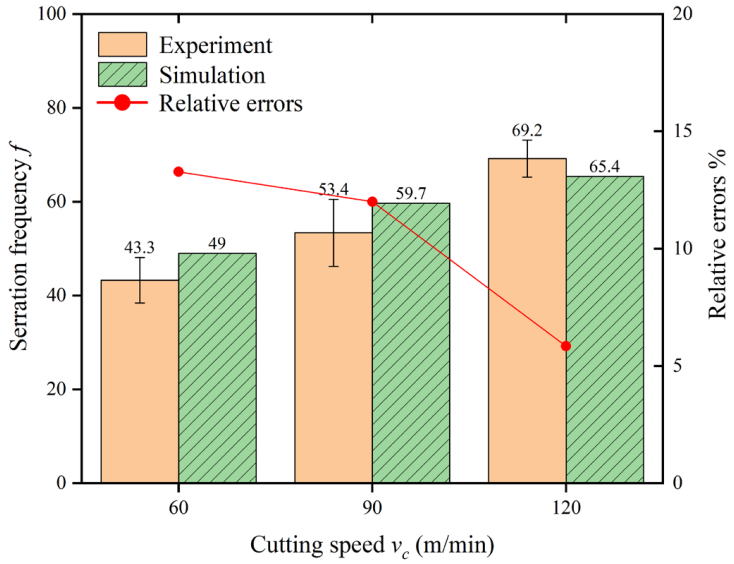

Figure 8. Comparison of the experimental and predicted chip serration frequency f.

4.3. Strain Rate

Figure 9 is the comparison between the experimental result and the simulation result of the strain rate field in the cutting deformation area. From Figure 9, compared with the distribution characteristics of the strain rate field obtained by the cutting experiment (the red high strain rate region is banded along the shear band), the strain rate distribution field obtained by the simulation has similar distribution characteristics. It is worth noting that with closer tool–workpiece contact, the strain rate becomes greater.

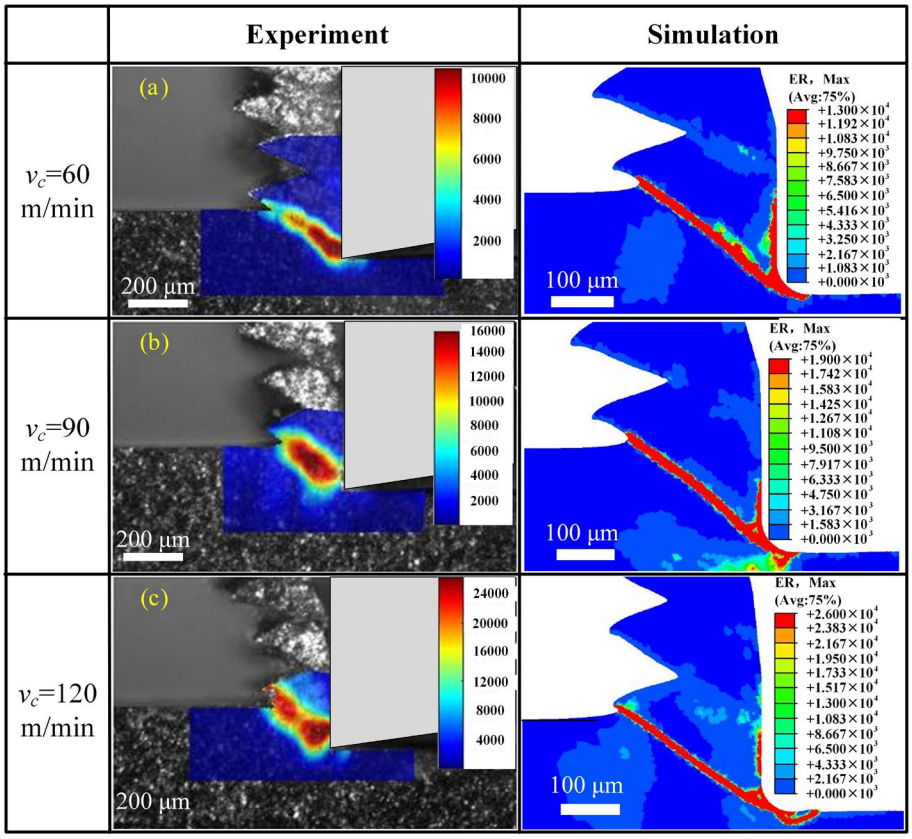

Figure 9. Comparison of experimental and predicted strain rate fields at different cutting speeds. (**a**) v_c = 60 m/min; (**b**) v_c = 90 m/min; (**c**) v_c = 120 m/min.

Figure 10 shows the comparison results and relative errors between the experimental maximum strain rate and the simulated maximum strain rate in the cutting deformation region. From Figure 10, the maximum strain rate of the cutting deformation area obtained by finite element simulation is slightly higher than that of the experimental strain rate at three cutting speeds, and the relative errors are 11.3%, 12.8%, and 5.45%, respectively. When the speed reached 90 m/min, the relative error of the maximum strain rate obtained by the simulation model is highest, which is 12.8%.

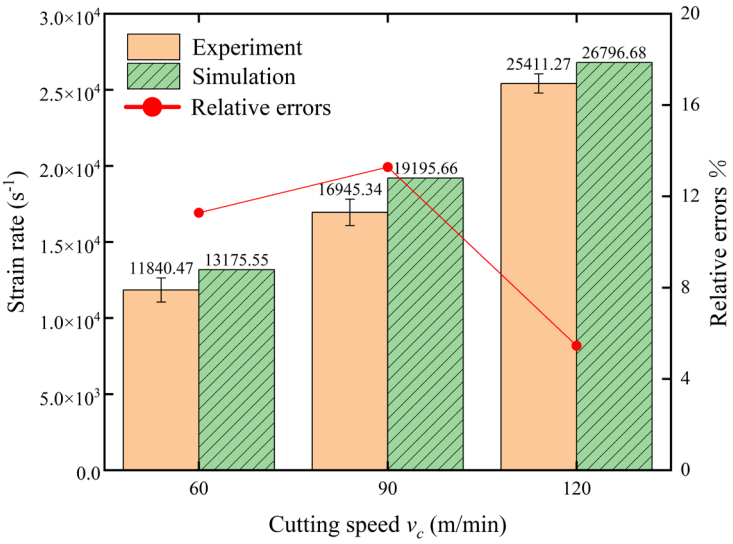

Figure 10. Comparison of the maximum strain rate in PSZ region between experiment and prediction.

5. Results

5.1. Temperature Field Characterization

Figure 11 is the cutting temperature distribution result with the formation of the sawtooth unit at 60 m/min. As shown in Figure 11, the high-temperature region of cutting deformation is consistent with the shear band region, and the temperature range is between 550 °C and 600 °C (red region). In the chip formation process, the shear zone is the main area of heat generation and accumulation. In the serrated chip initiation stage (Figure 11a), the slip of the shear band mainly occurs at the contact position between the tool tip and the workpiece, and the temperature of the contact point is the highest. In the 50% serrated chip formation stage (Figure 11b) and 75% serrated chip formation stage (Figure 11c), the shear band continues to slip and extend, and the higher temperature region also extends. When the serrated chip is completely formed (Figure 11d), an adiabatic shear band that penetrates the shear surface is formed, and the higher temperature region penetrates the entire shear surface.

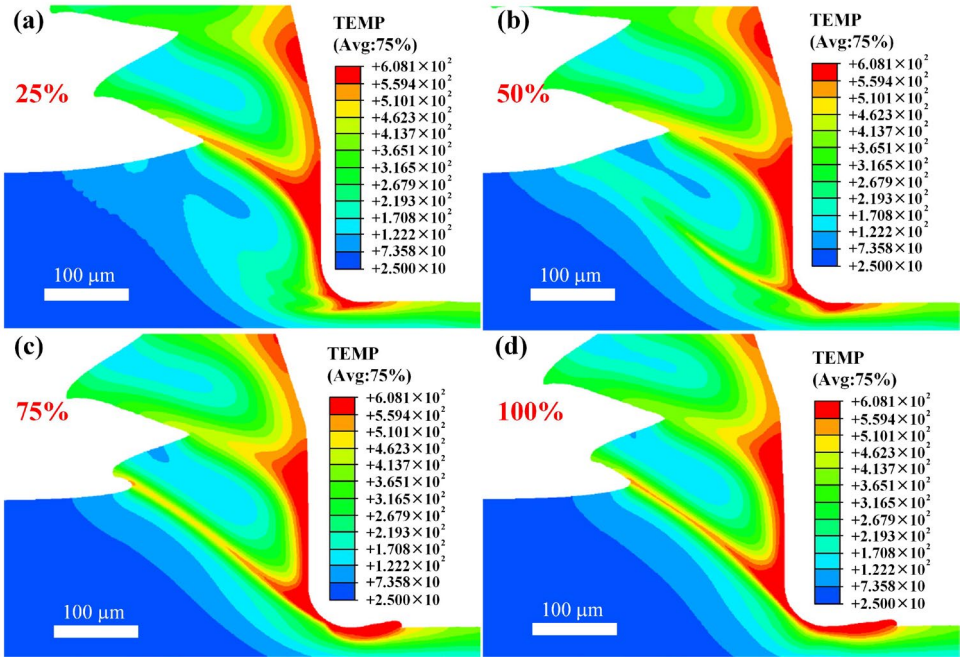

Figure 11. Cutting temperature changes with four stages of serrated unit formation (v_c = 60 m/min). (**a**) 25% serrated chip formation stage (initiation stage); (**b**) 50% serrated chip formation stage; (**c**) 75% serrated chip formation stage; (**d**) 100% serrated chip formation stage (serrated chip in completely formed stage).

Nine points evenly distributed on the adiabatic shear band path are selected to obtain the variation law of cutting temperature along the path, as shown in Figure 12. At the serrated chip initiation stage, the heat is mainly concentrated near the tool area, and the temperature of reference point 1 is the highest, which is 489 °C. Along the shear band path, the cutting temperature gradually decreases, and the temperature of reference point 9 is the lowest, which is 79 °C. In the 50% serrated chip formation stage and 75% serrated chip formation stage, the shear band extends, and the reference point temperature also increases. When the serrated chip is formed completely, a high-temperature zone that is consistent with the adiabatic shear band is formed through the shear plane, and the temperature is higher than 600 °C.

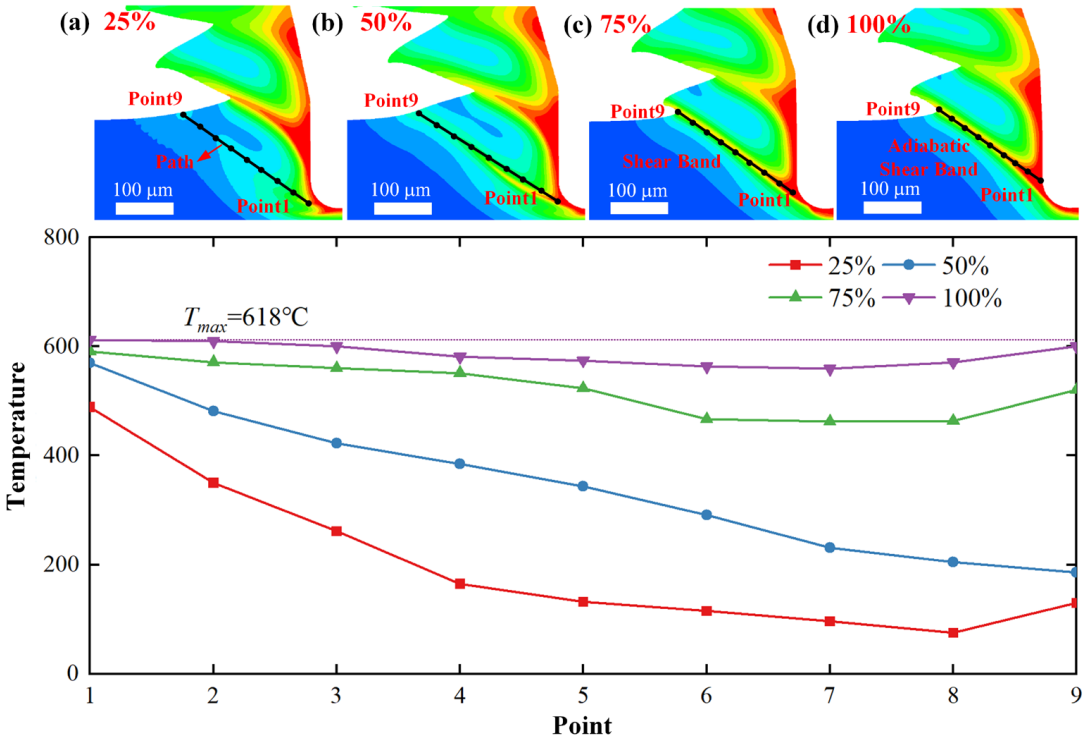

Figure 12. Evolution law of cutting temperature along the path under different serration formation stages (v_c = 60 m/min). (**a**) 25% serrated chip formation stage (initiation stage); (**b**) 50% serrated chip formation stage; (**c**) 75% serrated chip formation stage; (**d**) 100% serrated chip formation stage (serrated chip in completely formed stage).

5.2. Strain Field Characterization

Figure 13 is the strain distribution result at 60 m/min. In the serrated chip initiation stage and the 50% serrated chip formation stage, as shown in Figure 13a,b, the equivalent plastic strain of the material is low, and it is mainly concentrated near the tool–workpiece contact point, indicating that obvious plastic deformation occurred. As the cutting process continues, when 75% serrated chips are formed (Figure 13c), the high deformation region extends along the shear band extension direction, indicating that the material undergoes significant plastic deformation and flow in the shear band region. When the serrated chip is completely formed, as shown in Figure 13d, the high strain region runs through the entire shear surface, and the adiabatic shear region undergoes severe plastic deformation. In the serrated chip formation, the change of strain is consistent with the change of temperature, and the high plastic strain region extends correspondingly with the extension of the shear band.

Similarly, nine points evenly distributed on the adiabatic shear band path are selected to obtain the variation law of plastic strain along the path (Figure 14). In the serrated chip initiation stage, the plastic strain value is less than 1. In the 50% serrated chip stage and 75% serrated chip stage, plastic strain is significantly increased compared to the first stage, and the plastic strain value is the largest near the tool, which is 3.07 and 3.88, respectively. When the serrated chips are completely formed, the plastic strain values are greater than 3.66.

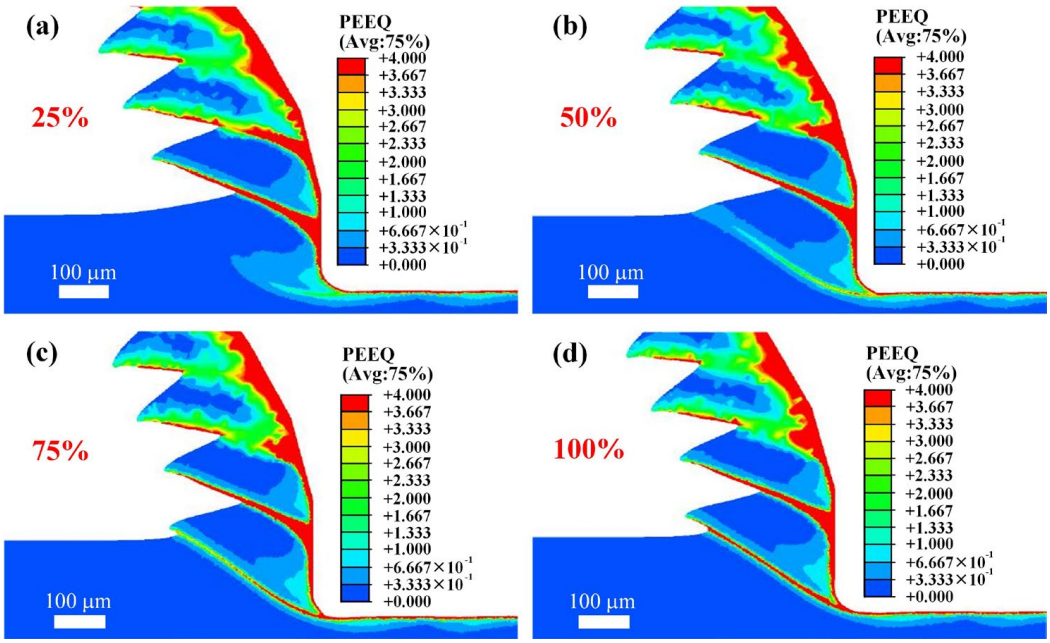

Figure 13. Distribution of strain with the formation stage of serrated elements (v_c = 60 m/min). (**a**) 25% serrated chip formation stage (initiation stage); (**b**) 50% serrated chip formation stage; (**c**) 75% serrated chip formation stage; (**d**) 100% serrated chip formation stage (serrated chip in completely formed stage).

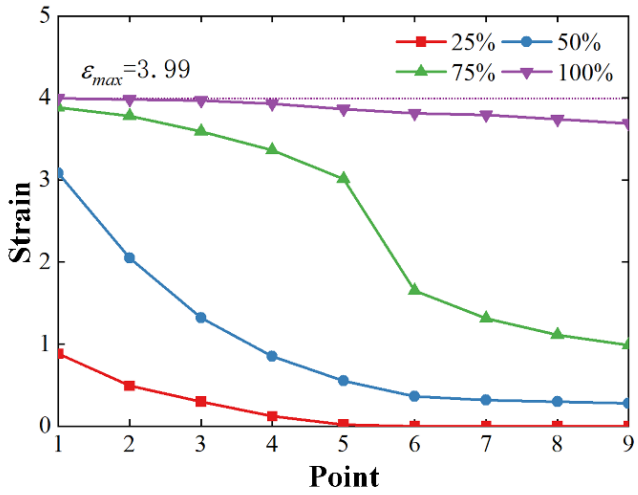

Figure 14. Evolution law of strain along the path under different serration formation stages (v_c = 60 m/min).

5.3. Strain Rate Field Characterization

Figure 15 is the change of shear strain rate distribution obtained by the simulation model at 60 m/min. In the serrated chip initiation stage (Figure 15a), the shear strain rate decreases gradually along the shear band from the blade edge. At the 50% serrated chip stage (Figure 15b), a high strain rate region extends along the shear band direction, showing a spatially non-uniform distribution of the shear strain rate. When the saw-tooth unit slips, that is, from 75% saw-tooth chips to the complete formation of saw-tooth chips (Figure 15c,d), the shear strain rate shows a uniform distribution trend.

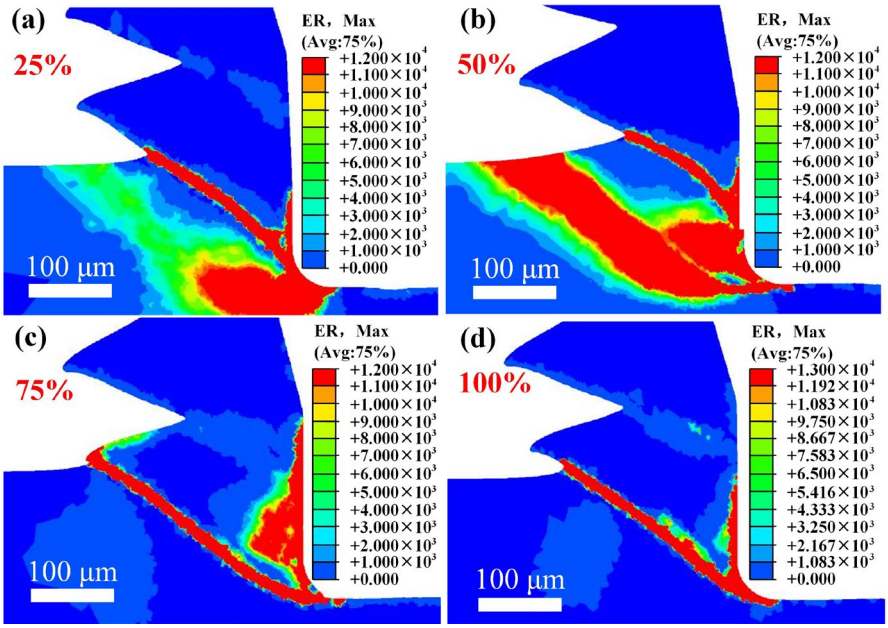

Figure 15. Strain rate changes with the formation stage of the serrated unit (v_c = 60 m/min). (**a**) 25% serrated chip formation stage (initiation stage); (**b**) 50% serrated chip formation stage; (**c**) 75% serrated chip formation stage; (**d**) 100% serrated chip formation stage (serrated chip in completely formed stage).

6. Discussion

The serrated chip formation process is divided into four stages, namely, 25% serrated chip stage, 50% serrated chip formation stage, 75% serrated chip formation stage, and 100% serrated chip formation stage. From the above simulation results, it can be seen that the adiabatic shear band plays a key role in the formation of serrated chips. With the advancement of the cutting process, the size and distribution of temperature, strain, and the strain rate in the adiabatic shear band area gradually evolve until a complete adiabatic shear band is formed, the shear fracture is completed, and finally the serrated chips are formed.

We analyze the formation of serrated chips in four stages. The 25% serrated chip stage is the initial stage of serrated chip formation. At this stage, with the increase in the extrusion effect of the tool on the material, the actual cutting layer thickness increases from 0, and the material does not produce obvious extrusion deformation, which is manifested as a slight protrusion of the free surface of the chip. With accumulation of shear extrusion, shear slip occurs, and the initial shear plane is formed in the shearing deformation zone. The temperature, strain, and strain rate on the initial shear plane begin to increase, and the flow stress begins to rise (Figures 11a, 13a and 15a). The process of generating 50% serrated chips is the second stage of serrated chip formation. This stage shows that the actual cutting thickness continues to increase, the surface of the machined layer is completely raised, the shear slip extends along the direction pointing to the free surface, and the initial shear surface also increases. At this time, the shear surface continues to extend, and thermal–mechanical loading of the shear plane continues to increase. Under the action of strain hardening and strain rate hardening, the flow stress continues to rise (Figures 11b, 13b and 15b). The production of 50% serrated chips is the third stage of serrated chip formation. At this time, the chip free surface is separated from the surface of the cutting layer, and the shear surface of the first deformation zone is formed. Under the action of high temperature, high strain, and a high strain rate (Figures 11c, 13c and 15c), some areas of the material reach a critical condition of dynamic recrystallization. Recrystallization causes flow stress to decrease, which causes plastic instability and leads to geometric instability of the initial shear surface. The chip morphology shows that the new serrated unit is

completely formed and gradually separated from the cutting layer. The fourth stage of serrated chip formation is the production of 100% serrated chips. At this stage, an adiabatic shear band throughout the shear surface is formed. Grains of the adiabatic shear band undergo complete dynamic recrystallization under the action of high temperature and strain rate. The flow softening caused by recrystallization makes the material on the whole shear surface completely plastically unstable, thus forming a new sawtooth unit. The new sawtooth element is completely separated along the shear plane, and the sawtooth element is about to leave the first deformation zone. At the same time, the next serrated unit enters the first stage, so that the reciprocation finally forms a continuous serrated chip (Figures 11d, 13d and 15d). Based on the above analysis of the influence of the thermal–mechanical loading field on serrated element formation, the formation mechanism of serrated chips is proposed (Figure 16).

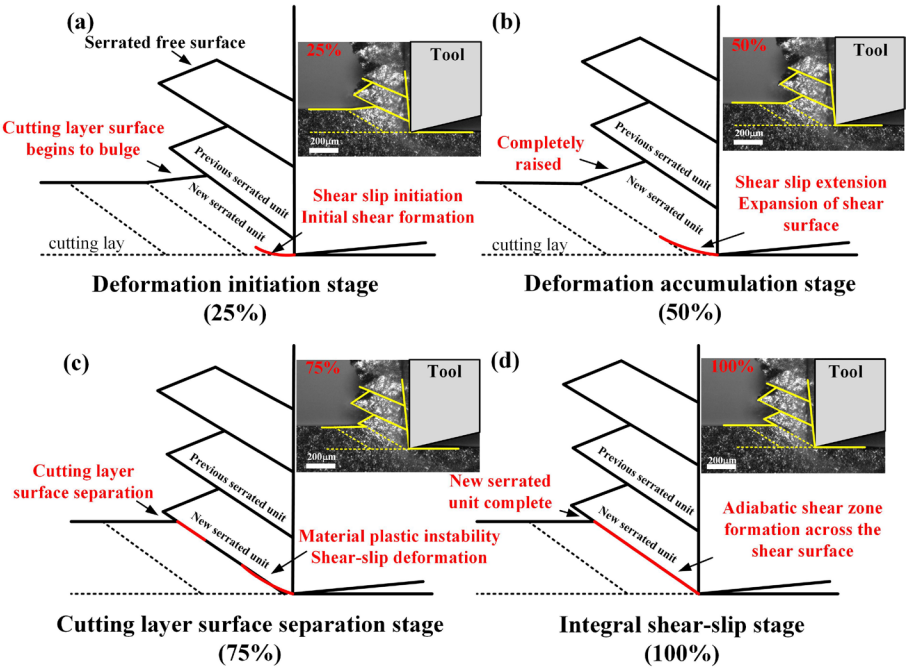

Figure 16. (**a**–**d**) Serrated unit forms a four-stage model diagram.

7. Conclusions

The finite element simulation model of the cutting process of FGH96 is established with a modified J–C constitutive model. Based on the verification of the simulation model, the variation of the thermal–mechanical loading field during the formation of serrated elements is characterized. The formation mechanism of serrated chips is proposed. The main conclusions are as follows.

1. The simulation model was verified by the cutting force, chip morphology, and strain rate using the orthogonal cutting experimental platform. For the cutting force, the maximum relative errors between the experimental average and the predicted average of the main cutting force F_c and the radial force F_p are 3.63% and 9.50%, respectively. Compared with the experimental values of the chip characterization parameters, the maximum relative errors of the tooth top height, tooth valley height, tooth spacing, tooth top angle, and tooth bottom angle are 2.24%, 11.4%, 6.48%, 3.12%, and 5.26%, respectively. For the strain rate, the simulation value of the maximum strain rate in the cutting deformation area is slightly higher than the experimental value, and the maximum error is 12.8%. In summary, the finite element simulation model has good predictability.
2. The variation law of serrated chip formation is revealed. During the serrated chip formation process, the temperature field, strain field, and strain rate field in the first

deformation zone show similar distribution characteristics to the distribution of shear bands, and the values gradually increase with the serrated chip formation process.

3. A formation model of serrated chips is proposed. Specifically, in the stage of serrated chip initiation, the material does not produce obvious extrusion deformation. As the shear surface continues to extend, the temperature, strain. and strain rate of the shear surface continue to increase during the generation of 50% serrated chips. At the stage of producing 75% serrated chips, the chips are separated from the surface of the cutting layer, and the shear surface of the first deformation zone is formed. The coupling effect of the temperature, strain, and strain rate on the shear band promotes dynamic recrystallization, which leads to complete plastic instability on the adiabatic shear band and then forms serrated chips with periodic distribution.

Author Contributions: Conceptualization, X.R.; Software, C.L.; Validation, Y.L.; Formal analysis, X.W.; Data curation, C.L.; Writing—original draft, X.R.; Writing—review & editing, B.W.; Project administration, Z.L.; Funding acquisition, X.R. All authors have read and agreed to the published version of the manuscript.

Funding: This research was funded by the National Natural Science Foundation of China (No. 52105460).

Institutional Review Board Statement: Not applicable.

Informed Consent Statement: Not applicable.

Data Availability Statement: Data is contained within the article.

Conflicts of Interest: The authors declare no conflict of interest.

References

1. Sreenu, B.; Sarkar, R.; Kumar, S.S.; Chatterjee, S.; Rao, G.A. Microstructure and mechanical behaviour of an advanced powder metallurgy nickel base superalloy processed through hot isostatic pressing route for aerospace applications. *Mater. Sci. Eng. A* **2020**, *797*, 140254. [CrossRef]
2. Thakur, A.; Gangopadhyay, S. State-of-the-art in surface integrity in machining of nickel-based super alloys. *J. Mach. Tools Manuf.* **2016**, *100*, 25–54. [CrossRef]
3. Thornton, E.L.; Zannoun, H.; Vomero, C.; Caudill, D.; Schoop, J. A Review of Constitutive Models and Thermal Properties for Nickel-based Superalloys Across Machining-Specific Regimes. *J. Manuf. Sci. Eng.* **2023**, *145*, 080801. [CrossRef]
4. Chen, G.; Caudill, J.; Ren, C.; Jawahir, I.S. Numerical modeling of Ti-6Al-4V alloy orthogonal cutting considering microstructure dependent work hardening and energy density-based failure behaviors. *J. Manuf. Process.* **2022**, *82*, 750–764. [CrossRef]
5. Xu, X.; Zhang, J.; Outeiro, J.; Xu, B.; Zhao, W. Multiscale simulation of grain refinement induced by dynamic recrystallization of Ti6Al4V alloy during high speed machining. *J. Mater. Process. Technol.* **2020**, *286*, 116834. [CrossRef]
6. Zang, J.; Zhao, J.; Li, A.; Pang, J. Serrated chip formation mechanism analysis for machining of titanium alloy Ti-6Al-4V based on thermal property. *Int. J. Adv. Manuf. Technol.* **2018**, *98*, 119–127. [CrossRef]
7. Uhlmann, E.; Von Der Schulenburg, M.G.; Zettier, R. Finite element modeling and cutting simulation of Inconel 718. *CIRP Ann.* **2007**, *56*, 61–64. [CrossRef]
8. Hao, Z.; Li, J.; Fan, Y.; Ji, F. Study on constitutive model and deformation mechanism in high speed cutting Inconel718. *Arch. Civ. Mech. Eng.* **2019**, *19*, 439–452. [CrossRef]
9. Zheng, Z.; Ni, C.; Yang, Y.; Bai, Y.; Jin, X. Numerical analysis of serrated chip formation mechanism with Johnson-Cook parameters in micro-cutting of Ti6Al4V. *Metals* **2021**, *11*, 102. [CrossRef]
10. Wang, B.; Liu, Z. Shear localization sensitivity analysis for Johnson–Cook constitutive parameters on serrated chips in high speed machining of Ti6Al4V. *Simul. Model. Pract. Theory* **2015**, *55*, 63–76. [CrossRef]
11. Ye, G.; Li, X.; Zhang, P.; Xue, S.; Zhang, Y.; Huang, X. The formation mechanism of discontinuously segmented chip in high speed cutting of Ti-6Al-4 V. *Int. J. Adv. Manuf. Technol.* **2023**, *130*, 1477–1493. [CrossRef]
12. Opoz, T.T.; Chen, X. Chip Formation Mechanism Using Finite Element Simulation. *J. Mech. Eng.* **2016**, *62*, 636–646. [CrossRef]
13. Aydın, M. Finite element modeling of high speed orthogonal cutting: A contribution to understanding the influence of mesh parameters on saw-toothed chip formation. *Proc. Inst. Mech. Eng. Part B J. Eng. Manuf.* **2023**, *9*, 1099–1110. [CrossRef]
14. Shen, X.; Zhang, D.; Yao, C.; Tan, L.; Li, X. Research on parameter identification of Johnson–Cook constitutive model for TC17 titanium alloy cutting simulation. *Mater. Today Commun.* **2022**, *31*, 103772. [CrossRef]
15. Calamaz, M.; Coupard, D.; Girot, F. A new material model for 2D numerical simulation of serrated chip formation when machining titanium alloy Ti–6Al–4V. *Int. J. Mach. Tools Manuf.* **2008**, *48*, 275–288. [CrossRef]
16. Rotella, G.; Umbrello, D. Finite element modeling of microstructural changes in dry and cryogenic cutting of Ti6Al4V alloy. *CIRP Ann.* **2014**, *63*, 69–72. [CrossRef]

17. Sima, M.; Özel, T. Modified material constitutive models for serrated chip formation simulations and experimental validation in machining of titanium alloy Ti–6Al–4V. *Int. J. Mach. Tools Manuf.* **2010**, *50*, 943–960. [CrossRef]
18. Kugalur-Palanisamy, N.; Rivière-Lorphèvre, E.; Ducobu, F.; Arrazola, P.J. Influence of the choice of the parameters on constitutive models and their effects on the results of Ti6Al4V orthogonal cutting simulation. *Procedia Manuf.* **2020**, *47*, 458–465. [CrossRef]
19. Hou, X.; Liu, Z.; Wang, B.; Lv, W.; Liang, X.; Hua, Y. Stress-strain curves and modified material constitutive model for Ti-6Al-4V over the wide ranges of strain rate and temperature. *Materials* **2018**, *11*, 938. [CrossRef] [PubMed]
20. Ling, C.; Ren, X.; Wang, X.; Li, Y.; Liu, Z.; Wang, B.; Zhao, J. Dynamic Mechanical Properties and Modified Johnson-Cook Model Considering Recrystallization Softening for Nickel-Based Powder Metallurgy Superalloys. *Materials* **2024**, *17*, 670. [CrossRef] [PubMed]
21. Xu, X.; Outeiro, J.; Zhang, J.; Xu, B.; Zhao, W.; Astakhov, V. Machining simulation of Ti6Al4V using coupled Eulerian-Lagrangian approach and a constitutive model considering the state of stress. *Simul. Model. Pract. Theory* **2021**, *110*, 102312. [CrossRef]
22. Qiu, B.; Zhu, Y.; Ding, W. An investigation on material removal mechanism in ultra-high-speed grinding of nickel-based superalloy: Three-dimensional simulation and experimental verification. *Int. J. Adv. Manuf. Technol.* **2020**, *110*, 919–933. [CrossRef]